

A *CHANDRA* STUDY OF THE STELLAR X-RAY EMISSIVITY OF GLOBULAR CLUSTERS
IN M31 BULGE

XIAO-JIE XU

School of Astronomy and Space Science, Key Laboratory of Modern Astronomy and Astrophysics, Nanjing
University, Nanjing, P. R. China 210046

ZHIYUAN LI

School of Astronomy and Space Science, Key Laboratory of Modern Astronomy and Astrophysics, Nanjing
University, Nanjing, P. R. China 210046

ABSTRACT

The X-ray emissivity (i.e., luminosity per unit stellar mass) of globular clusters are an important indicator of their dynamical evolution history. Based on deep archival *Chandra* observations, we report a stacking analysis of 44 globular clusters (GCs) with 0.5-8 keV luminosities $L_X \lesssim 10^{35}$ erg s⁻¹ in the M31 bulge, which are supposed to be dominated by cataclysmic variables (CVs) and coronally active binaries (ABs). We obtain a significant detection at 5σ level in 0.5-8 keV band. The average X-ray luminosity per GC and the average X-ray emissivity are determined to be $5.3 \pm 1.6 \times 10^{33}$ erg s⁻¹ and $13.2 \pm 4.3 \times 10^{27}$ erg s⁻¹ M_⊙⁻¹, respectively. Both of these values are consistent with those of MW GCs. What's more, the measured emissivity of M31

GCs is also consistent with that of the MW field stars. Massive GCs have X-ray luminosities which are marginally higher with less massive ones. Massive GCs also show a lower emissivity ($4.5 \pm 2.4 \times 10^{27} \text{ erg s}^{-1} M_{\odot}^{-1}$) than less massive ones ($15.0 \pm 7.8 \times 10^{27} \text{ erg s}^{-1} M_{\odot}^{-1}$), which is consistent with the scenario that the (progenitors of) CVs and ABs were more efficiently destructed via stellar encounters in the more massive GCs. No dependence of the X-ray emissivity on GC color or on the projected galactocentric distance of GCs were found.

Keywords: globular clusters: general – X-rays: binaries – galaxies: M 31

1. INTRODUCTION

Globular clusters (GCs) in our Galaxy are rich in stellar X-ray sources. The identified sources include (quiescent) low-mass X-ray binaries ((q)LMXBs), millisecond pulsars (MSPs), cataclysmic variables (CVs) and coronally active binaries (ABs). These sources are mostly located inside the half-light radius (r_h) of GCs (e.g., [Di Stefano et al. 2002](#); [Pooley et al. 2003](#); [Kim et al. 2006](#); [Zhang et al. 2011](#); [D’Ago et al. 2014](#); [Cheng et al. 2017](#)). Compared to the Galactic field, GCs in both the Milky Way (MW) and external galaxies were found to have much higher chances to host LMXBs with a luminosity $L_X \gtrsim 10^{35}$, which are thought to be formed via close stellar encounters in the crowded environment in GCs ([Fabian & Pringle 1975](#); [Pfahl et al. 2002](#); [Pooley et al. 2003](#); [Ivanova et al. 2005, 2008](#); [Hurley et al. 2007](#); [Fregeau et al. 2009](#); [Bahramian et al. 2013](#); [Agar & Barmby 2013](#)). The majority of GCs, on the other hand, have L_X below $10^{34-35} \text{ erg s}^{-1}$, which are supposed to be dominated by CVs and ABs (e.g., [Pooley et al. 2003](#); [Cheng et al. 2017](#)). Compared to LMXBs, the progenitors of CVs and ABs are less massive and have a longer evolution timescale. Hence, dynamical

xuxj@nju.edu.cn

lizy@nju.edu.cn

processes are also expected to affect the formation of CVs and ABs in GCs. Indeed, previous work (e.g., [Pooley et al. 2003](#); [Pooley & Hut 2006](#); [Maxwell et al. 2012](#)) revealed a correlation between the number of weak X-ray sources detected in GCs and the so-called stellar encounter rate, which was interpreted as evidence for a dynamical origin for such sources, in particular CVs. However, stellar interactions, including two-body and three-body encounters, should take place with competing effects, in which binaries can be created in two-body interactions, but also can be destroyed or modified in three-body interactions ([Hut et al. 1992](#)). In this regard, whether the number of CVs and ABs could be effectively elevated by the stellar encounters in GCs remains an open issue.

One way of testing the net outcome of the dynamical interactions is to compare the X-ray emissivities (luminosity per unit stellar mass, ε_X) of GCs with that of field stars. Recently, we carried out such a study on 69 MW GCs, obtaining an average ε_X of $\sim 7.3 \pm 2.7 \times 10^{27}$ erg s⁻¹ M_⊙⁻¹ in the 0.5-8 keV band ([Cheng et al. 2017](#)). This is found to be lower than the field level, which is represented by CVs and ABs detected in the Solar neighborhood and the cumulative X-ray emission from gas-poor dwarf elliptical galaxies in the Local Group ($\sim 12 \times 10^{27}$ erg s⁻¹ M_⊙⁻¹; [Sazonov et al. 2006](#); [Ge et al. 2015](#); [Cheng et al. 2017](#)). This provides strong evidence for dynamical destruction of the progenitors of CVs and ABs, due chiefly to binary-single interactions in GCs ([Cheng et al. 2017](#)).

It is desired to extend the above study to GCs in other galaxies. However, unlike the luminous LMXBs (with $L_X \gtrsim 10^{36}$ erg s⁻¹) that have been routinely detected in external galaxies ([Fabbiano 2006](#)), the weak X-ray populations studied in [Cheng et al. \(2017\)](#), when placed at extragalactic distances, are beyond the detection sensitivity of current X-ray facilities. Moreover, even a single LMXB with $L_X \approx 10^{35}$ erg s⁻¹ can easily mask the cumulative X-ray emission from the numerous CVs and ABs in the same host GC. In this regard, Local Group galaxies are perhaps the only laboratory to study the properties of weak X-ray sources in GCs. In particular, M31, the nearest massive galaxy with a large GC population, is the best-suited target. M31 has been observed by

Chandra for more than 100 times with an accumulated exposure approaching 1 Ms. This ensures a source detection limit down to a few times 10^{34} erg s $^{-1}$ in its bulge, thus allowing for a clean identification of GCs hosting bright LMXBs (Kong et al. 2002; Fan et al. 2005; Peacock et al. 2010; Barnard et al. 2014) and opening up the opportunity of measuring the cumulative emission from the fainter stellar populations, i.e., CVs and ABs.

In this work, we present a study on confirmed GCs in the M31 bulge with individual L_X below the *Chandra* detection limit, by performing a stacking analysis. The stacking technique has been proved powerful to detect the cumulative X-ray emission of faint, unresolved sources to enable the study of their average properties, e.g., X-ray luminosities of high-redshift galaxies (e.g., Zinn et al. 2012; Basu-Zych et al. 2013). Recently, Vulic et al. (2014), in a study primarily focusing on the resolved X-ray binaries in the bulge and disk of M31, performed a stacking analysis on 54 GCs, which was reported to be a non-detection at an upper limit of $\sim 10^{32}$ erg s $^{-1}$ GC $^{-1}$. However, this is a puzzling result, in regard with the typical luminosity of a few 10^{33} erg s $^{-1}$ found in the MW GCs (e.g., Cheng et al. 2017), and is to be contrasted with our present study.

The remainder of this paper is organized as follows. We introduce the data and analysis method in § 2 and present the results in § 3. We discuss the implications of the results and conclude in § 4. Throughout this work we adopt a distance of 780 kpc for the M31 GCs, and a Galactic foreground absorption column density of $N_H = 7.0 \times 10^{20}$ cm $^{-2}$. Quoted errors are at 90% confidence level, unless otherwise stated.

2. DATA & ANALYSIS

2.1. X-ray Data Preparation

The central $\sim 8'$ region of M31 is one of the most frequently visited targets of *Chandra*. For our purpose, we utilize 122 publicly available ACIS observations taken between 1999 to 2013 (including

81 ACIS-I and 12 ACIS-S observations), which were primarily for monitoring the X-ray binary populations in the bulge (e.g., Barnard et al. 2014). Individual level 1 data files from each observation were reprocessed to produce the level 2 data files using CIAO v.4.5 and the corresponding calibration files, following the standard pipeline. For the ACIS-S observations, we used only data taken from the S2 and S3 CCDs. Counts, exposure and point-spread function (PSF, defined as 90% encircled energy radius) maps in the 0.5-2 (S), 2-8 (H), and 0.5-8 (F) keV bands were created. A first run of the CIAO tool *wavdetect* was employed to detect and locate sources in each observation. We then corrected for the relative astrometry of each observation with respect to ObsID 1575, which has the longest exposure, by matching centroids of the commonly found bright sources. The counts and exposure maps were reprojected to produce the final, merged images. The PSF maps were also merged, individually weighted by the exposure map at a given pixel. The total effective exposure exceeds 700 ks in the central $\sim 2'$ and gradually decreases to a value of ~ 400 ks at radii out to $8'$. The merged *Chandra* 0.5-8 keV image is presented in Figure 1.

wavdetect was employed a second time on the merged images to detect sources in all three bands. Our final source list consists of 406 independent sources inside $8'$. Further studies of these sources will be presented elsewhere (see also Vulic et al. 2016 for an updated *Chandra* catalog of X-ray sources in M31). We inspected the sensitivity map produced in *wavdetect* and found that the local detection limit reaches 6.0×10^{-5} cts s^{-1} within a galactocentric radius of $2'$ and gradually decreases to 2.0×10^{-4} cts s^{-1} at $8'$. Assuming a fiducial absorbed power-law spectrum with a photon-index of 1.7, we obtain a count rate-to-intrinsic luminosity conversion factor of 9.1×10^{38} erg $s^{-1}/(\text{cts } s^{-1})$ in the 0.5-8 keV band, and the above limits translate to 0.55×10^{35} erg s^{-1} and 1.8×10^{35} erg s^{-1} , respectively. The latter is set as the global detection limit for subsequent analysis. (There are two GCs which were below the detection limit, but were detected in the central region since the detection limit is lower in that region. However, they were both excluded from the stacking list because there

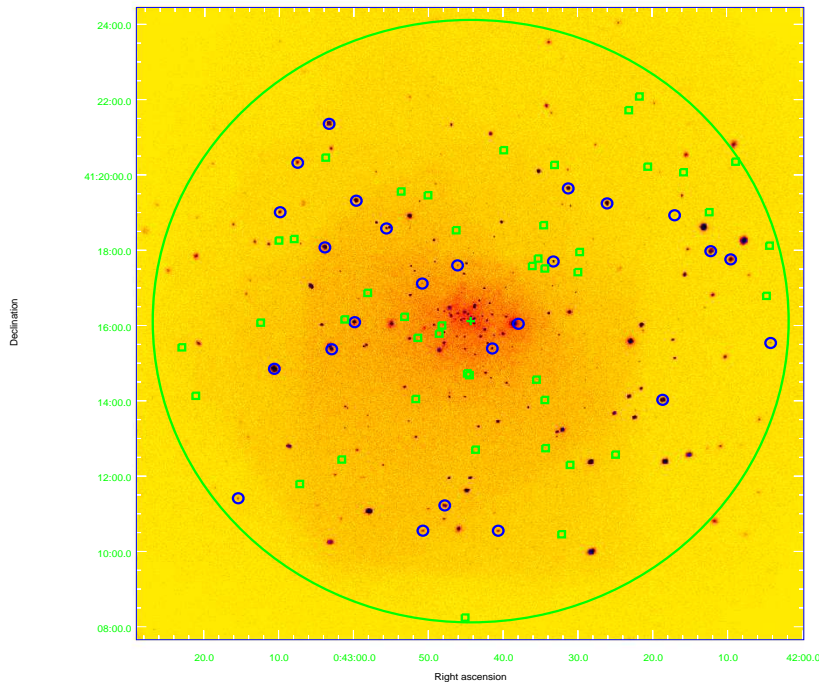


Figure 1. 0.5-8 keV merged *Chandra* ACIS image of the M31 bulge, overlaid by 25 X-ray-detected (blue circles) and 44 non-detected (green squares) GCs. The latter are included in stacking analysis. The large circle measures a galactocentric radius of $8'$, while the cross marks the M31 center. (Some of the GCs were contaminations near them.)

2.2. GC Sample Selection

The stacking analysis requires a sample of GCs with L_X below the detection limit of the merged *Chandra* observations, since any detected X-ray counterpart is expected to be dominated by LMXBs. We start from the Revised Bologna Catalogue of M31 globular clusters V.5 by [Galleti et al. \(2004, <http://www.bo.astro.it/M31/>\)](#) and the GC list by [Peacock et al. \(2010\)](#). As the first step, only confirmed GCs within $8'$ from the M31 center are included to make a balance between the number of GCs and the increasing PSF size. This leads to a preliminary sample of 81 GCs. Next, this sample is cross-correlated with our X-ray source list. An X-ray source is considered to be associated with a GC if their projected offset is within $1''$ or two times the source positional uncertainty, whichever is larger. A total of 25 GCs are thus found with an X-ray counterpart (marked as circles in Figure

1). The mean offset of 22 out of the 25 pairs is found to be $0.19 \pm 0.10''$. The other three pairs, located at far off-axis, show large offsets of $\sim 5''$, which could be chance alignments. These 25 GCs, along with an addition of 11 GCs located within 3 times the 90% PSF of a nearby X-ray source, are excluded from further analysis. As the last step, we visually examine the vicinity of the remaining 45 GCs and further remove 1 GC that could still be contaminated by nearby bright X-ray sources. Our final sample of 44 GCs are presented in Table 1 and marked by squares in Figure 1.

2.3. Stacking Analysis

The stacking analysis is restricted to a 20-pixel \times 20-pixel ($\sim 10'' \times 10''$) square region centering at the individual sample GCs. It is straightforward to stack the counts map (C map) and exposure map in the F, S and H bands. The effective exposure in the stacked map is $E = 19$ Ms, with negligible variation within the small area. In addition, we make stacked maps for a control field, namely shifting the 44 boxes by a distance of 20 pixels in a source-free, otherwise random direction.

To determine the average net count rate, we consider the central 6-pixel \times 6-pixel box of the C map as the source region and the rest of the C map as the background region. The size of the source region, which obviously affects the net count rate, is chosen for the following considerations. Ideally, the source region should be large enough to enclose stars located with the half-light radius (r_h). Unfortunately, most of our sample GCs do not have r_h available in the literature (see Table 1). Therefore we take the well determined r_h of MW GCs (Harrison 2010), and calculate their apparent half-light radii when placed at the distance of M 31. In this way, the characteristic r_h of the M 31 GCs is estimated to be $0''.76 \pm 0''.42$, or 1 – 3 ACIS pixels. Considering the relative astrometric uncertainty in the X-ray source/GC catalogs, as well as the increased PSF size at far off-axis, a 6-pixel \times 6-pixel box is a reasonable choice. Moreover, this choice is also supported by the the profile of stacked count map in § 3.

Table 1. Basic properties of sampled GCs.

GC Name	R.A.	Dec.	r_h	m_v	$\log M$	$m_b - m_v$	D
			($''$)		(M_\odot)		($'$)
B075	10.536767	41.339236	-	17.33	5.51	0.92	7.89
B080	10.551537	41.316914	-	17.442	5.46	1.221	6.65
B091	10.590458	41.368167	-	17.56	5.14	0.80	7.31
B093	10.596392	41.362103	-	16.87	5.64	0.97	6.86
B103	10.623879	41.299339	-	15.23	6.3	1.02	3.29
B104	10.624883	41.290433	-	17.51	5.21	0.77	2.99
B106	10.629317	41.205108	-	16.03	6.03	0.96	4.58
B109	10.634029	41.174408	0.8	16.22	5.58	1.12	6.12
B114	10.642929	41.212514	0.89	17.28	5.38	0.42	3.88
B115	10.64335	41.233853	0.46	16.03	6.25	1.02	2.82
B119	10.650337	41.293164	-	17.408	5.28	0.94	2.12
B126	10.682004	41.211861	-	17.149	5.32	0.77	3.43
B127	10.685408	41.244836	1.45	14.467	6.45	0.49	1.45
B132	10.714196	41.26135	0.27	17.739	5.07	0.92	1.41
B134	10.715325	41.234283	0.41	16.57	5.6	0.91	2.50
B136	10.723529	41.326144	-	17.005	5.64	0.97	3.85
B145	10.756588	41.207469	0.29	18.1	5.12	0.32	4.92
B152	10.791733	41.304386	-	16.16	5.82	0.91	5.27
B154	10.801896	41.268022	-	16.758	5.9	0.95	5.29
B167	10.838017	41.235592	0.46	17.41	5.29	1.02	7.20
B169	10.845838	41.257042	-	17.08	6.24	1.23	7.30
B262	10.708542	41.324478	-	17.605	5.2	0.79	3.50
B264	10.721621	41.270667	0.32	17.577	5.13	1.00	1.67
B268	10.779967	41.196614	0.37	18.314	4.95	1.00	6.11
NB16	10.637892	41.337892	-	17.55	5.23	0.66	4.64
NB17	10.643329	41.292061	-	18.922	4.60	0.71	2.32
B053D	10.603958	41.209639	-	19.761	4.26	0.88	5.10
NB29	10.647079	41.296439	-	18.821	4.64	1.23	2.36
NB35	10.643963	41.311214	-	19.627	4.32	0.92	3.13
NB39	10.702287	41.263217	0.75	17.941	4.99	0.28	0.87
NB41	10.70075	41.266833	-	18.097	4.93	0.35	0.74
NB89	10.686579	41.245614	-	17.965	4.98	0.12	1.41
AU010	10.742179	41.281242	-	17.506	5.17	0.98	2.69
B040D	10.517892	41.302036	-	18.811	4.64	0.69	7.78
B041D	10.519667	41.279817	-	18.319	4.97	1.26	7.47
B064D	10.64805	41.242839	-	16.47	5.94	0.74	2.28
B068D	10.66625	41.344422	-	18.652	4.71	0.90	4.60
B090D	10.754983	41.269497	-	17.373	5.47	0.98	3.17
BH23	10.765679	41.341106	0.32	18.828	4.64	0.74	5.66
B523	10.692829	41.308997	-	18.677	4.70	0.90	2.43

3. RESULTS

The counts inside the defined source region are summed to give the count numbers of the source, while the background is determined by the averaged counts in the background region (blue line in Figure 2, see following description for details on the background determination). Then the net count number is calculated by:

$$C_N = C_S - C_B \times A_S/A_B ,$$

where C_N , C_S , C_B , A_S and A_B are net counts, counts of the source and the background regions, area of the source and background regions, respectively.

In Figure 2 we present the stacked net C maps of all 44 GCs in F, S, H bands and the control group in F band. The images were smoothed for plotting only. There are 1023 counts (F band) in the source region of the C map, and the respective total background counts in the source region is 871 counts. This revealed a source with $(1023 - 871)/\sqrt{871} \sim 5\sigma$ significance in F band. Similar detections occur in S ($\sim 4\sigma$) and H ($\sim 2\sigma$) bands. The average count rates and luminosities of sampled GCs are given in Table 2. The errors of the values is a combination of Poisson error of the source count number, the background count number, and a 10% additional error to account for the uncertainties brought by background determination and count rate to flux conversion. Comparing to previous detection limit of $\sim 1.4 \times 10^{35} \text{ergs s}^{-1}$ (F band, the same hereafter), the stacking results in an averaged luminosity of $5.3 \pm 1.6 \times 10^{33} \text{ergs s}^{-1} \text{GC}^{-1}$. This is more than an order of magnitude improvement. As comparison, non-detection was found for the control stacking regions.

In Figure 3, the count number profile of the merged C map were plotted (black dots). From the figure, the count distribution has a peak at the center pixels and drops to a near-constant value outside 3 pixels, which were considered as background (blue line). As a result, even an increment of source region to 10×10 pixel box does not result in any increase in net count rate or luminosity.

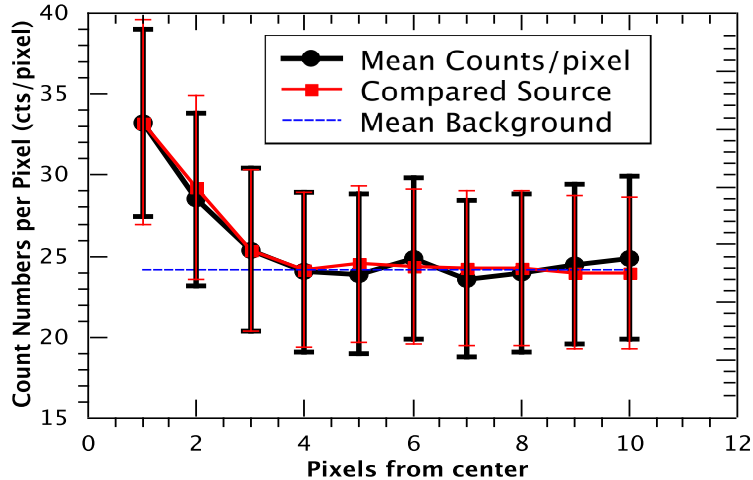


Figure 2. Stacked count profile of the sample GCs in the 0.5-8 keV band, shown by the black dots and black solid line. The blue horizontal line marks the background level determined by averaging the count numbers outside the central 6×6 pixels. The red squares and red line are the counts profile obtained by stacking 10 detected sources, normalized to have the same counts in the center pixel as the GC profile.

Therefore, we conclude that our choice of the source region is reasonable. For comparison, the merged count profile of a randomly selected sample of 10 detected sources is also presented in Figure 2 (the profile was normalized so that it has the same count numbers at the center pixels with merged GCs). These 10 sources were randomly chosen within $8'$ of M31 center and have count rates within 10 times the detection limit. It is clear that both merged maps have similar count distribution: the count profiles drop to a quasi-constant level outside 3 pixels. We again conclude that the sizes of source and background region is reasonable.

Table 2. X-ray count rates, X-ray luminosities and X-ray emissivities of stacked GCs.

Bands/Groups	net count rate (10^{-6} ctss $^{-1}$ GC $^{-1}$)	L_X (1.0×10^{33} erg s $^{-1}$ GC $^{-1}$)	ϵ_X (1.0×10^{27} erg s $^{-1}$ /M $_{\odot}$)
All GCs			
F	7.4 ± 2.2	5.3 ± 1.6	13.2 ± 4.3
S	5.6 ± 1.9	2.9 ± 1.0	7.3 ± 2.5
H	1.7 ± 1.1	1.9 ± 1.3	4.8 ± 3.2
Subgroups of GCs			
F,log $M > 6.0$	11.9 ± 6.4	8.4 ± 4.5	4.5 ± 2.4
F,log $M < 6.0$	4.4 ± 2.3	3.1 ± 1.6	15.0 ± 7.8
MW GCs			
F,all GCs	–	3.8 ± 0.6	7.3 ± 2.7
F,log $M > 6.0$	–	14.4 ± 1.0	5.6 ± 2.9
F,log $M < 6.0$	–	2.8 ± 0.5	14.6 ± 9.3

Note.-Column 1: Stacking Bands or sub groups of GCs. Column 2:0.5-8 keV count rate. Column 3: 0.5-8 keV X-ray luminosity. Column 4: Specific X-ray emissivity of GCs.

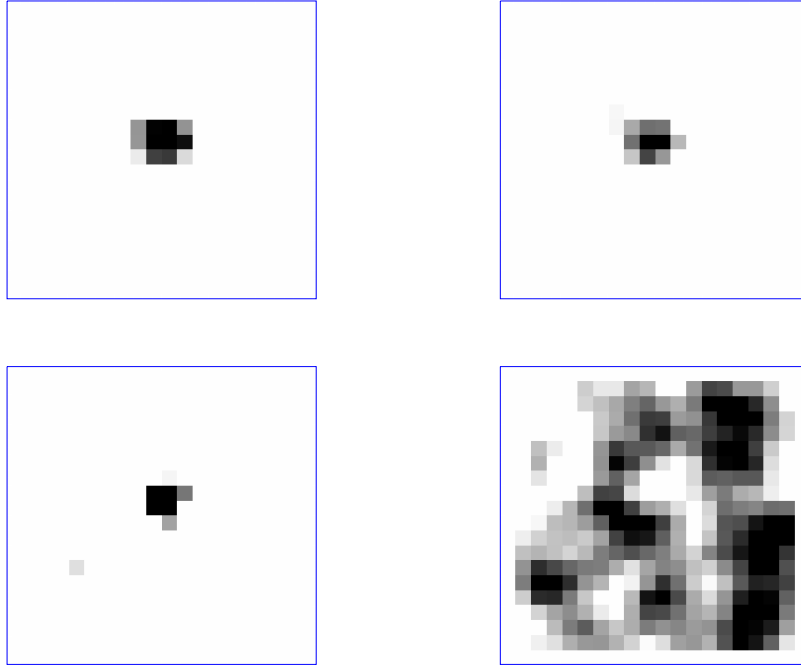


Figure 3. Stacked count maps for sampled GCs in F band (upper left), S band (upper right), H band (lower left) and control field in F band (lower right). The maps are smoothed by a 2-pixel Gaussian kernel for enhanced illustration only.

The net count rates are then calculated as C_N/E , where E is the respective mean exposure time from the exposure map. The flux and luminosity for each band is calculated by assuming an absorbed power law spectrum. The slope Γ of the spectrum was assumed to be 1.7, which is typical for MW GCs and is consistent with the H/S count ratio of 0.4. The count rate to flux conversion factor is then determined to be $1.25 \times 10^{-11} \text{ erg s}^{-1} \text{ cts s}^{-1}$ from the assumed power law spectrum. We choose the Poisson error to represent the uncertainties of the count numbers in source and background regions and calculate the other uncertainties accordingly.

As the next step, the specific X-ray emissivity ε_X of sampled GCs is calculated by $\varepsilon_X = L_X/M_{\text{avg}} = 13.2 \pm 4.3 \times 10^{27} \text{ erg s}^{-1} M_{\odot}^{-1}$, where L_X is the averaged X-ray luminosity of sampled GCs, and the averaged mass (M_{avg}) of GCs were adopted from [Ma et al. \(2015\)](#) and the uncertainties of the GC masses have been included. As the next step, the sampled GCs are divided into two groups according to their masses. Group 1 GCs have $\log M/M_{\odot} > 6.0$ and Group 2 GCs have $\log M/M_{\odot} \leq 6.0$. Stacking is then performed for each group and the results are also listed in [Table 2](#). Apparently, more massive GCs on average have lower ε_X than less massive ones. But their X-ray luminosities are only marginally higher than those less massive ones. Additionally, stacking analysis are performed on sub groups of GCs according to their color (represented by $m_B - m_V$) or the distance to M31 center and no apparent dependences are found.

4. DISCUSSION & CONCLUSION

Our stacking has a valid detection on $\sim 5 \sigma$ level. In contrary, a similar stacking work by [Vulic et al. \(2014\)](#) found no valid detection. Comparing with [Vulic et al. \(2014\)](#)'s paper, we suspect that there are two possible reasons to be responsible. The first one is the astrometry correction step before merging more than 100 *Chandra* observations. For example, we used *reproject_aspect* command in *CIAO* to compare positions of detected sources and make corrections to the aspect files

before merging (We have noticed that the correction step was also included in a later paper by the same group of authors, e.g., [Vulic et al. 2016](#)). This correction can reduce up to 85% source residuals (typically ~ 0.2 to $0.8''$) and could be crucial when merging more than 100 *Chandra* observations. For comparison, such a step is missing in the description of [Vulic et al. \(2014\)](#), and the `reproject_obs` command were directly used to merge the observations before correcting astrometry in [Vulic et al. \(2014\)](#). Another possible reason could be the different star cluster catalog used in the two works. [Vulic et al. \(2014\)](#) used PHAT year 1 cluster catalog (see [Johnson et al. 2012](#)) for stacking, while the revised Bologna catalog is used in this work. The former catalog is concentrated on the disk region, while the latter catalog covers the whole M31 region. As a result, the two catalog contain GCs with different properties which could lead to different stacking results.

The average count rate of our sampled GCs reaches $7.4 \pm 2.2 \times 10^{-6} \text{cts s}^{-1} \text{GC}^{-1}$ in F band, which is an order of magnitude lower than the detection limit. The average L_X ($5.3 \pm 1.6 \times 10^{33} \text{erg s}^{-1} \text{GC}^{-1}$) of sampled GCs is consistent with the average L_X of the MW GCs ($3.8 \pm 0.6 \times 10^{33} \text{erg s}^{-1} \text{GC}^{-1}$, see [Cheng et al. 2017](#)).

The (marginally) higher average X-ray luminosity of massive GCs than less massive ones is as was found in the MW GCs, and can be naturally explained by more primordial binary star systems in massive GCs ([Cheng et al. 2017](#)). However, their lower ε_X suggests that CVs and/or ABs are less abundant in massive GCs than less massive ones. A similar trend was also found in MW GCs ([Cheng et al. 2017](#)). Based on a sample of 69 MW GCs, [Cheng et al. \(2017\)](#) proposed that the binary-single and binary-binary stellar encounters are more efficient in massive GCs, which would destroy (the progenitors of) CVs and ABs more effectively and reduce their numbers which leads to lower ε_X . Similar mechanism could also be responsible for the lower ε_X in M31 GCs. Unfortunately, we are unable to determine the stellar encounter parameter Γ for M31 GCs due to the lack of knowledge on dynamical parameters of sampled GCs. We suggest further observations on M31 GCs to test this

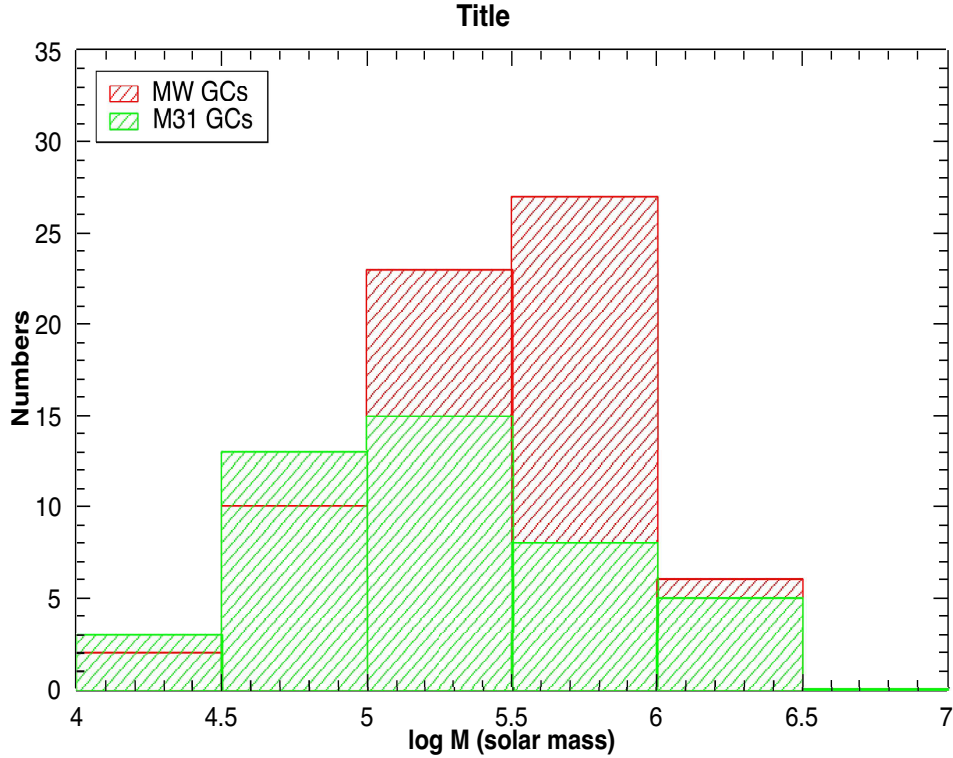


Figure 4. The mass distribution of sampled GCs. Green histograms are M31 GCs, and red ones are the MW GC sample from [Cheng et al. \(2017\)](#).

possibility.

Our measurements do not suggest a lower emissivity of M31 GCs than that of the MW field stars. The measured specific emissivity of M31 GCs ($\varepsilon_X = 13.2 \pm 4.3 \times 10^{27} \text{erg s}^{-1} M_{\odot}^{-1}$) is consistent with both that of MW GCs ($\varepsilon_X = 7.3 \pm 2.7 \times 10^{27} \text{erg s}^{-1} M_{\odot}^{-1}$, [Cheng et al. 2017](#)), and of MW field stars ($\sim 12 \times 10^{27} \text{erg s}^{-1} M_{\odot}^{-1}$; [Sazonov et al. 2006](#); [Ge et al. 2015](#)). Given the lower mean mass of M31 GCs comparing to MW GCs (see Fig 4), the apparent consistency may be broken by further investigation.

Our results do not suggest the dependence of L_X per cluster on either the distance of GCs to M31 center, or $m_B - m_V$, the color of GCs. It is possible that such dependences are relatively minor comparing to the mass and dynamical histories of M31 GCs, as was found in MW GCs ([Cheng et al. 2017](#)), which requires further study. What's more, the dynamical encounter rates and therefore the X-ray emitting source population in M31 GCs are not necessarily similar to those of the MW GCs,

which will depend on future observations. Last but not least, the sampled GCs in this research are located in M31 bulge, so they may have been experienced more dynamical evolution than typical globular clusters in M31 (e.g., [Agar & Barmby 2013](#)), or be atypical of the overall population in other ways. Thus the overall emissivity of M31 GCs requires further investigations.

The authors thank the anonymous referee for constructive comments that helped improve this paper. This work is supported by National Science Foundation of China through grants NSFC-11303015, 11473010, and NSFC-11133004, the National Key Research and Development Program of China (2016YFA0400803), NSFC-11773015 and NSFC-11133001.

Facilities:

Facility: CXO (ACIS).

REFERENCES

- Agar, J. R. R.; Barmby, P., 2013, *AJ*, 146, 135
Bahramian, Arash, Heinke, Craig O., Sivakoff, Gregory R., & Gladstone, Jeanette C., 2013, *ApJ*, 766, 136
Barnard, R. et al., 2014, *ApJ*, 780, 83
Basu-Zych A. R. et al., 2013, *ApJ*, 762, 45
Binney, J., & Merrifield, M., 1998, *Galactic Astronomy* (Princeton, NJ: Princeton Univ. Press)
Chatterjee, A., Fregeau, J. M., Umbreit, S., & Rasio, F. A., 2010, *ApJ*, 719, 915
Cheng, Z-Q., Li, Z-Y., Xu, X-J., & Li, X-D, 2017, submitted to *ApJS*
D'Ago, G. et al., 2014, *A&A*, 567, 2
Di Stefano, R. et al., 2002, *ApJ*, 570, 618
Fabian, A. C., Pringle, J. E., & Rees, M. J., 1975, *MNRAS*, 172, 15
Fan, Z. et al, 2005, *PASP*, 117, 1236
Fregeau, J M., Ivanova, N., Rasio, F A., 2009, *ApJ*, 707, 1533
Galleti, S. et al., 2004, *A&A*, 416, 917
Ge, C., Li, Z-Y., Xu, X., Gu, Q-S., et al. 2015, *ApJ*, 812, 130
Hurley, J. R., Aarseth, S. J., & Shara, M. M., 2007, *ApJ*, 665, 707
Ivanova, N., Belczynski, K., Fregeau, J. M., & Rasio, F. A., 2005, *MNRAS*, 358, 572
Ivanova, N. et al., 2006, *MNRAS*, 372, 1043
Ivanova, N., Heinke, C. O., Rasio, F. A., Belczynski, K., & Fregeau, J. M., 2008, *MNRAS*, 386, 553
Ivanova, N., 2010, *AIPC*, 1314, 143 (arXiv:1101.2864)
Kim, E. et al., 2006, *ApJ*, 647, 276
Kong, A. K. H. et al., 2002, *ApJ*, 577, 738
Kundu, A., Maccarone, T., Zepf, S. E., & Puzia, T. H., 2003, *ApJ*, 589, L81
Lehmer, B. D. et al., 2008, *ApJ*, 681, 1163
Ma, J., Wang, S., Wu, Z-Y., et al. 2015, *AJ*, 149, 56
Maxwell, J. Edward, Lugger, Phyllis M., Cohn, Haldan N., et al. 2012, *ApJ*, 756, 147
Peacock, M. B. et al., 2012, *MNRAS*, 402, 803
Peacock, M. B., Maccarone, T. J., Kundu, A., & Zepf, S. E., 2010, *MNRAS*, 407, 2611
Pfahl, E., Rappaport, S., & Podsiadlowski, P., 2002, *ApJ*, 573, 283
Pooley, D. et al., 2003, *ApJ*, 591, L131
Pooley, David, & Hut, Piet, 2006, *ApJL*, 646, L143
Sazonov, S., Revnivtsev, M., Gilfanov, M. et al, 2006, *A&A*, 450, 117
Shirey, R. et al., 2001, *A&A*, 365, L195
Vulic, N., Barmby, P., & Gallagher, S. C., 2013, *ApJ*, 763, 96
Vulic, N., Gallagher, S. C., & Barmby, P., 2014, *ApJ*, 790, 136
Vulic, N., Gallagher, S. C., & Barmby, P., 2016, *MNRAS*, 461, 3443
Zhang, Z. et al., 2011, *A&A*, 533, 33
Zinn, P.-C., Blex, S., Seymour, N., & Bomans, D. J., 2012, *A&A*, 547, 50
Johnson, L. Clifton, Seth, Anil C., Dalcanton, Julianne J. et al., 2012, *ApJ*, 752, 95